Geometrically Controlled Mechanically Responsive Polyelectrolyte Tube Arrays

*Lin Han, Lifeng Wang, Khek-Khiang Chia, Robert E. Cohen, Michael F. Rubner, Mary C. Boyce, and Christine Ortiz**

Over the last two decades, there has been extensive work on stimulus-responsive materials and structures that undergo actuation, swelling, variable permeability and wettability, and aggregation in the presence of external environmental stimulus, e.g., pH, ionic strength, temperature, and pressure.[1–4] However, the design, fabrication, characterization, and fundamental understanding of mechanically responsive, or "mechanomutable", materials that change their mechanical properties in response to external stimuli are still in relatively early stages.[5–12] In this study, the coupling between inherent material properties and deformation mechanisms known to take place for anisotropic geometries, such as bending, buckling, and twisting, are explored in order to tune mechanical responsiveness. High-resolution atomic force microscopy (AFM)-based nanoindentation experiments are utilized to quantify and study the responsive mechanical behavior of cylindrical polyelectrolyte tube arrays. The experimental results are compared to the predictions of microstructurally specific finite element models, which probe the underlying deformation mechanisms, based on our previous model considering bending and buckling of individual tubes.[13] The results demonstrate that geometry can be used to systematically vary mechanomutability in this model system. Such mechanically responsive systems hold great potential for use as dynamic substrates for fundamental studies of cell behavior, control of particle transport in microfluidic devices and on substrates, morphing structures, switchable shock absorbers, and autonomous motion.

The model material system chosen for this study is an ionically complexed polyelectrolyte multilayer (PEM) of poly(allylamine hydrochloride) (PAH) and poly(acrylic acid) (PAA). This PEM undergoes a reversible pH-dependent transition, described in detail previously,[14–17] and hence, possesses inherent mechanically responsive behavior that originates at the molecular level. At low pH (2.0), the polyelectrolyte network is highly swollen,[15] owing to nearly complete protonation of the PAA carboxylate groups and the resulting low level of ionic pairing (cross-linking) compared to higher pH (5.5). When the pH is increased from 2.0 to 5.5, the increased concentration of negatively charged carboxylate groups on the PAA chains leads to extensive ionic pairing with positively charged amines on the PAH chains to form a highly cross-linked, significantly less swollen network.[15] Therefore, the inherent mechanical behavior of this material is expected to depend on the ionic cross-link density, the net charge density, the presence of molecular entanglements, and the volume fraction of water. The PEM tube forests were fabricated on planar substrates with cylindrical holes by conformal layer-by-layer assembly of 10, 15, and 20 PAH/PAA bilayers (where one bilayer (BL) consists of one monolayer of PAA and one monolayer of PAH) on track-etched polycarbonate membranes, which were utilized as sacrificial templates[15,18] (see Experimental Section). Because the tube forests were assembled from the outer cylindrical surface inwards, increasing the number of bilayers deposited resulted in a decrease in the inner diameter of the tubes (**Table 1**). Planar PAH/PAA films consisting of 70 bilayers were also prepared for comparison. The geometric structural parameters of the planar films and tube forests (e.g., height, outer and inner radii, and packing density) were measured experimentally via fluorescence microscopy and AFM imaging at pH 2.0 and 5.5, 0.01 M ionic strength (**Figure 1**a and Table 1). The statistical distribution of the geometric parameters was quantified thoroughly (Table 1) and the effect of this structural heterogeneity on the mechanical behavior was assessed (as discussed later on). The experimental maximum contact area was ≈70 μm^2 for pH 5.5 (containing ≈15 tubes) and ≈200 μm^2 for pH 2.0 (containing ≈60 tubes), thereby providing reasonably homogenized effective mechanical responses for the tube assemblies.

AFM-based nanoindentation (see Experimental Section) was employed to quantify the mechanical responsiveness of the PEM planar films and tube forests using a non-adhesive colloidal probe that had been functionalized with a hydroxyl-terminated self-assembled monolayer, at constant indentation depth rates (Figure 1b) and in force relaxation at constant indentation depth (Figure 1c). Values of the effective indentation modulus, E_{ind}, at all the tested indentation rates and at equilibrium were calculated from these data via the substrate-corrected Hertz model (Figure 1d).[19] These data showed that both the planar films and tube forests exhibited significant pH-dependent mechanically responsive behavior. The magnitude of the "mechanomutability" was defined as the ratio of E_{ind} at the two different pHs, $E_{ind,\ pH\ 5.5}/E_{ind,\ pH\ 2.0}$ (Figure 1e).

Dr. L. Han, Prof. M. F. Rubner, Prof. C. Ortiz
Department of Materials Science and Engineering
Massachusetts Institute of Technology
Cambridge, MA 02139, USA
E-mail: cortiz@mit.edu
Dr. L. Wang, Prof. M. C. Boyce
Department of Mechanical Engineering
Massachusetts Institute of Technology
Cambridge, MA 02139, USA
Dr. K.-K. Chia, Prof. R. E. Cohen
Department of Chemical Engineering
Massachusetts Institute of Technology
Cambridge, MA 02139, USA

DOI: 10.1002/adma.201102917

Table 1. Summary of pH-dependent dimensions of PAH/PAA polyelectrolyte multilayer tube forests (10, 15, and 20 bilayers) and planar film (70 bilayers) dimensions (mean ± standard deviation for $n \geq 200$ measurements). Planar film thickness was measured by selective removal and contact mode AFM. Tube forest measurements were carried out by fluorescence microscopy after immersion in a suspension of fluorescent-red carboxylate-modified polystyrene beads, where average tube center-to-center distance, w, was measured to be 1.8 ± 0.3 μm by estimating the local tube density within a 10 μm × 10 μm square box ($n = 100$).

pH	System	inner diameter d_{in} [μm]	outer diameter d_{out} [μm]	tube height/film thickness H [μm]
5.5	10 BL tube forest	0.58 ± 0.10	1.16 ± 0.16	12.04 ± 1.02
	15 BL tube forest	0.49 ± 0.16	1.16 ± 0.20	12.05 ± 0.47
	20 BL tube forest	0.36 ± 0.11	1.17 ± 0.18	12.17 ± 0.57
	planar film	–	–	2.09 ± 0.07
2.0	10 BL tube forest	0.86 ± 0.27	1.70 ± 0.30	17.80 ± 1.05
	15 BL tube forest	0.82 ± 0.26	1.77 ± 0.25	17.94 ± 0.74
	20 BL tube forest	0.48 ± 0.25	1.81 ± 0.29	18.01 ± 1.03
	planar film	–	–	8.27 ± 0.52

For the planar films, the origin of the observed mechanomutability was the inherent material responsiveness due to molecular-level structural, conformational, and chemical changes that accompany the pH-dependent macromolecular transition.[15] E_{ind} at pH 5.5 was observed to be greater than E_{ind} at pH 2.0, presumably due to increased ionic cross-link density, which offsets any stiffness lost by the decreased net charge density, and hence, electrostatic repulsion.[15] $E_{ind,\ pH\ 5.5}/E_{ind,\ pH\ 2.0}$ ranged between ≈100–1000× for the planar films (comparing filled and open diamond symbols, Figure 1d), and between ≈2–80× for the tube forests, which depended greatly on geometry, as quantified in this case by the tube cross-sectional area (Figure 1e). At both pHs, the tube forests were observed to be markedly more compliant than the planar films (Figure 1d), except for the 20-bilayer system at pH 2.0, which exhibited similar indentation behavior to the planar film (open triangle and open diamond symbols, Figure 1d). Furthermore, E_{ind} of both the planar films and tube forests were found to be indentation rate-dependent, and this rate dependence was much greater for pH 5.5 compared to pH 2.0 (Figure 1d).

Figure 1c plots the normalized time-dependent force relaxation at pH 2.0 and 5.5 for the planar film compared to the tube forests. The magnitudes of the equilibrium effective indentation modulus, E_{ind}, calculated from these data (Figure 1d) are orders of magnitude different for the planar film and tube forests. However, the time-dependent relaxation trend was similar for both systems at the same pH, indicating that this phenomenon is dominated by the inherent responsive material properties, irrespective of geometry (Figure 1c). Possible contributions to this observed rate- and time-dependent mechanical behavior include breaking and reforming of the ionic cross-links, intrinsic viscoelasticity of the solid macromolecular component, and fluid flow-governed poroelasticity.[20] The magnitudes of the force relaxation were observed to be much greater for the more highly cross-linked, less hydrated PEMs at pH 5.5 (≈55 vol% water) compared to those at pH 2.0 (≈90 vol%). At pH 5.5, local rupture of amine–carboxyl ionic cross-links can occur within the deformation zone during the force relaxation period,[21] thereby resulting in reduced compression resistance. In comparison, at pH 2.0, this effect can be reduced by the lower ionic cross-link density[22] and greater degree of hydration. The additional electrostatic repulsion from the net positive charge at pH 2.0 within the network also adds to the elastic component, and hence, is expected to further decrease the extent of viscoelasticity.

In order to explore the underlying deformation mechanisms of the experimentally observed geometry-dependent mechanical responsiveness of the PEMs, a microstructurally specific finite element analysis (FEA) indentation model was employed (see Experimental Section), which incorporates the inherent material stiffness represented by E_{ind} of the planar films, and the tube assembly geometry obtained from the fluorescence microscopy images (Table 1). For the planar film, at both pHs (2.0 and 5.5), the indentation results in a typical continuum multiaxial stress and strain field characteristic of classical Hertzian contact, regardless of the indentation depth and physical state, although it is somewhat substrate-constrained (**Figure 2**a). At pH 5.5, the simulation reveals the deformation mechanisms in the tube forests, which provide the significantly more compliant behavior when compared to the planar film (Figure 1d). In this case, where the majority of tubes are not in lateral contact, this increased compliance is due to a dual deformation field that takes place within the contact area with an outer low stress zone, which induces discrete tube compression and bending, and an inner high-stress zone resulting from initial tube buckling followed by tube bending (Figure 2a), similar to the nanoindentation responses of carbon nanotube forests without initial inter-tube contact.[13,23,24] At pH 2.0, the swollen 10-bilayer tubes still have a small enough cross-sectional area whereby most neighboring tubes are not initially in contact at zero load. Hence, the mechanical behavior is also dominated by discrete tube compression, bending, or buckling (Figure 2a). At pH 2.0, for the 15- and 20-bilayer tube forests, the cross-sectional area is increased enough that all tubes are initially in physical lateral contact with each other at zero load, which provides stress transfer between tubes, and hence, leads to a

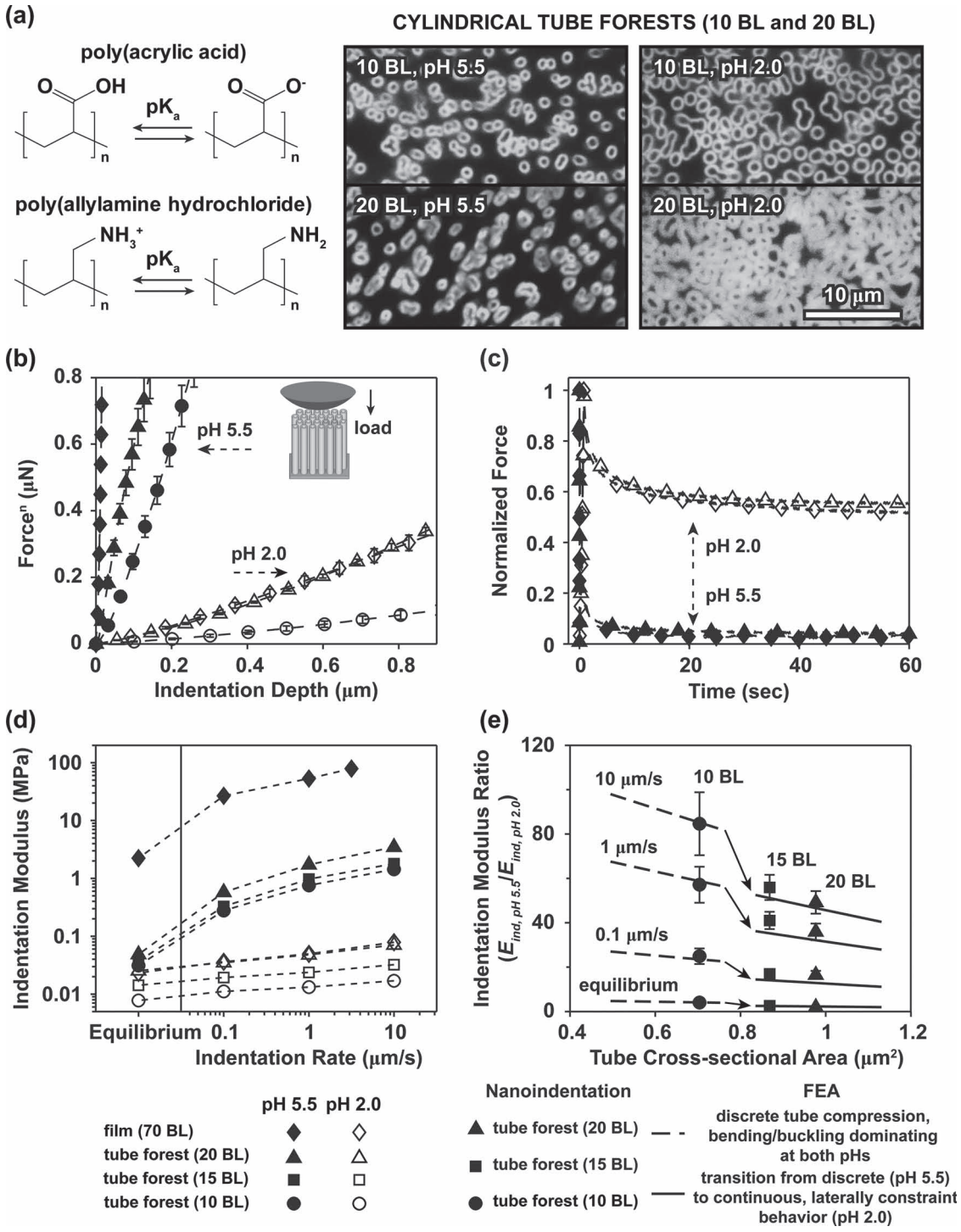

Figure 1. Mechanically responsive indentation behavior of PAH/PAA polyelectrolyte multilayer tube forests and planar films. a) pH-induced molecular-level interactions of PAH and PAA and corresponding fluorescence microscopy images of the tube forests at pH 5.5 and 2.0 (top view). b) Continuous-loading indentation at a constant indentation depth rate (1 μm s^{-1}), substrate-corrected force[19] (Force^n) versus indentation depth D. c) Average force relaxation curves after continuous-loading indentation at a constant indentation depth, normalized to the maximum force for each curve. d) Indentation modulus, E_{ind}, versus indentation rates dD/dt, where the dashed lines are to guide the vision. e) Experimentally measured and finite element analysis (FEA) predicted indentation modulus responsiveness ratio ($E_{ind,\ pH\ 5.5}/E_{ind,\ pH\ 2.0}$) as a function of tube cross-sectional area ($n \geq 10$ locations, mean ± standard error of the mean (SE) in (b,e), and SE is less than the size of data symbols in (c,d)).

more continuous and stiffer mechanical behavior and stress field similar to the planar film (Figure 2a), consistent with the experimental data (Figure 1d).

While varying the thickness of the planar film does vary the degree of substrate constraint, it does not change the fundamental Hertzian deformation mechanisms and origins of

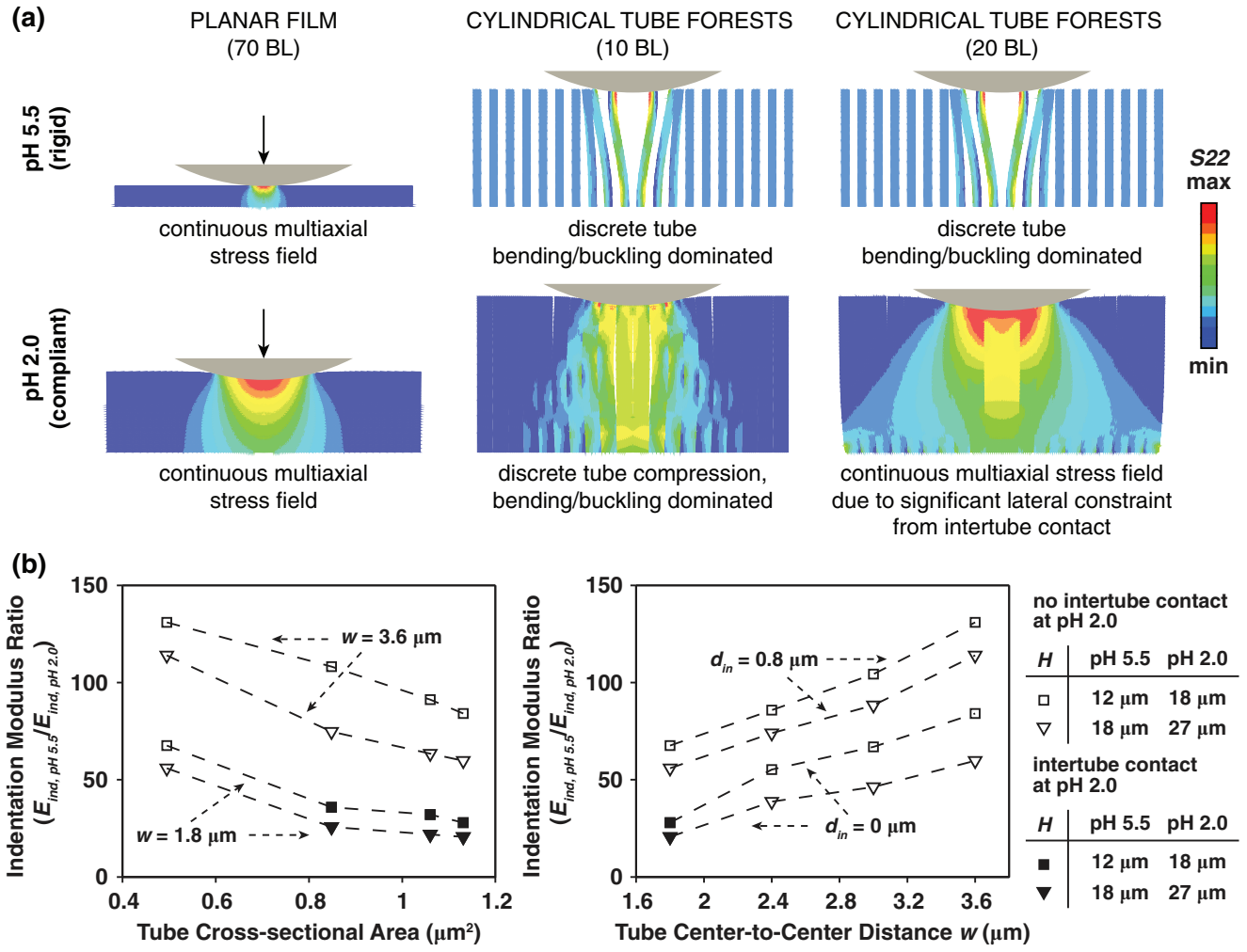

Figure 2. Mechanical responses of planar films and geometrically controlled mechanomutable tube forests by indentation FEA simulations. a) FEA predictions of mechanomutable deformation mechanisms for the film and tube forests, as shown in stress field *S22* contours (normal to the indentation direction). b) Indentation modulus responsiveness ratio ($E_{ind,\ pH\ 5.5}/E_{ind,\ pH\ 2.0}$ at 1 μm s^{-1} indentation rate) as a function of tube cross-sectional area at pH 5.5 and tube center-to-center distance *w* for two different tube heights, assuming constant tube outer diameter d_{out} = 1.2 μm at pH 5.5, and increases to 1.8 μm at pH 2.0.

mechanical responsiveness (Figure 2a). However, for the tube forests, the deformation mechanisms (Figure 2a), and hence, mechanical responsiveness vary markedly with geometry. FEA simulations are able to also quantitatively predict the experimentally observed mechanical responsiveness ratios for the tube forests as a function of geometry, as represented by the tube cross-sectional area (dashed and solid lines compared to symbols, Figure 1e). The FEA simulations predict a distinct mechanistic transition from a continuous multiaxial stress field at relatively high tube cross-sectional areas, or dense forests (solid lines, Figure 1e), to discrete tube compression bending and buckling at relatively low tube cross-sectional areas, or sparse forests (dashed lines, Figure 1e). This transition results in an amplification in the magnitude of the mechanical response ratio for sparser tube forests with decreasing tube cross-sectional area and lateral constraints (solid lines compared to dashed lines, Figure 1e). More detailed parametric studies show how the effective mechanical responsiveness of the tube forests can be engineered over a relatively wide range by tailoring different geometrical parameters (i.e., tube height, *H*, inner and outer diameter, d_{in} and d_{out}, cross-sectional area, A_{tube}, and center-to-center distance, *w*). For example, tube forests with different d_{out} and *w* were found to undergo drastically different stress distribution and deformation mechanisms upon indentation at different pHs (Figure 2b).

It should be noted that the orders of magnitude differences in mechanical behaviors of the tube forests compared to the planar film (Figure 1d) cannot be accounted for solely by a reduction in material surface area coverage or continuity; geometrically induced deformation mechanisms (Figure 2a) are needed to quantitatively predict the mechanical behaviors of the tube system (dashed and solid line compared to symbols, Figure 1e). **Figure 3** further explores this topic. Figure 3a compares the indentation force-depth behavior for 1) the planar film

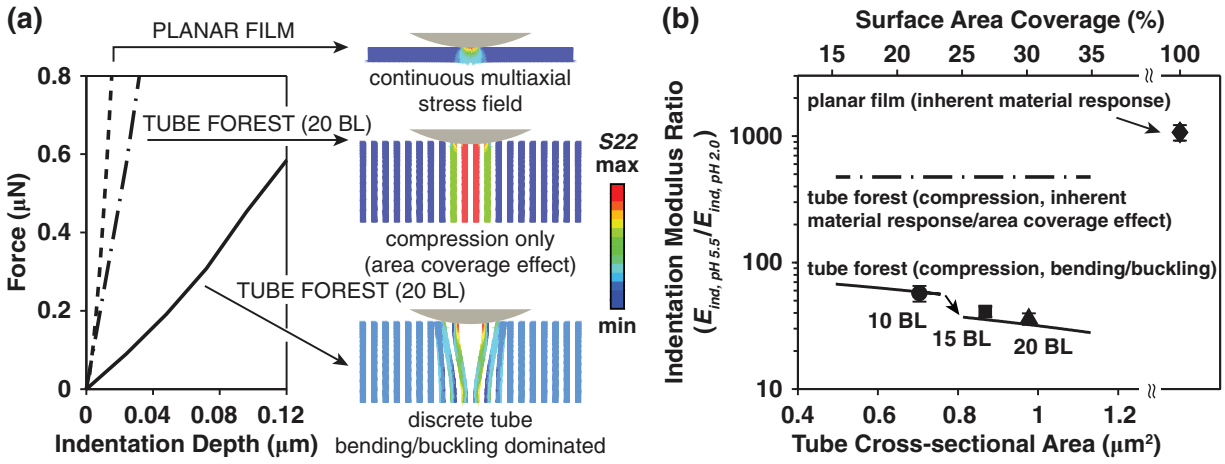

Figure 3. Comparison of the inherent materiality area coverage effect to the geometrically controlled deformation for PAH/PAA PEMs. a) FEA simulations of indentation force-depth curves and stress field *S22* contours (normal to the indentation direction) for the planar film (inherent material properties), the 20 BL tube forest with restricted compression only (inherent material properties including area coverage effect), and the 20 BL tube forest including geometrically induced bending and buckling deformation mechanisms. b) Indentation modulus responsiveness ratio ($E_{ind, pH 5.5}/E_{ind, pH 2.0}$ at 1 μm s^{-1} indentation rate) as a function of surface area coverage for the planar film (inherent material response) at 100% surface area coverage (experimental data, diamond symbol), the tube forest restricted to compression only (inherent material response, surface area coverage effect, dashed line, estimated from experimental data) and the tube forest including geometrically induced bending and buckling mechanisms (experimental data are symbols, solid lines are FEA simulations).

under compression, which reflects the inherent material properties; 2) the tube forest restricted to compression only, showing the area coverage effect and again only probing inherent material properties; and 3) the tube forest allowing geometrically induced bending and buckling deformation mechanisms. The indentation modulus, E_{ind}, calculated from these data for the tube forests under restricted compression only was found to be reduced to ≈0.3 of the planar solid film, which is in agreement with that calculated from the reduction in material surface area coverage. E_{ind} for the tube forests including bending and buckling deformation mechanisms is ≈0.03 of the planar film and one order of magnitude smaller than the compression-only simulations resulting from the reduction in area coverage. These results indicate that the geometrically induced bending and buckling mechanisms significantly increase the compliance of the tube forest system, much more so than the area coverage effect. Figure 3b plots the indentation modulus ratio or mechanical responsiveness ratio ($E_{ind, pH 5.5}/E_{ind, pH 2.0}$) as a function of surface area coverage again for the planar film, the tube forest excluding geometric effects (compression only), and the tube forest including geometrically induced deformation mechanisms (bending and buckling). As mentioned above, the planar film (100% surface area coverage) under compression represents the inherent material response (diamond symbol, Figure 3b). For the tube forests only under compression (i.e., excluding geometrically induced bending and buckling deformation mechanisms), the mechanical responsiveness ratio remains as a constant value with area coverage, reduced by ≈44% relative to the inherent film mutability (dashed line in Figure 3b). The experimentally measured data for the tube forests (symbols in Figure 3b, shown in more detail in Figure 1e) are one order of magnitude lower than that calculated for the inherent material response of the tube forest solely taking into account the area coverage effect (dashed line in Figure 3b). Hence, FEA simulations predict that the tubes exceed the critical buckling load and geometrically induced bending and buckling deformations, resulting from the cylindrical tube structure, are needed to account for the mechanical responsiveness.

The role of geometric heterogeneity (measured experimentally, Figure 1a and Table 1) was also explored using parametric FEA simulations, which assess the sensitivity of the mechanical behavior to the tube packing density, as represented by the tube center-to-center distance, the tube tilt angle and the differential tube height (Table 1). The predicted variability of the mechanical simulation results with added geometric heterogeneity was consistent with the magnitude of the experimental standard deviations reported (Figure 1), and hence, does not influence all of the major conclusions of the study.

This paper has demonstrated that mechanomutability can be controlled through the coupling between the "inherent" molecular-level material properties and the anisotropic microscale geometry in a cylindrical PEM model system (**Figure 4**). A unique geometrically controlled transition is discovered that amplifies mechanomutability due to a change in deformation mechanism from a continuous multiaxial stress field with lateral constraints due to inter-tube contact, to discrete tube compression, bending, and buckling with decreasing tube cross-sectional area. The fundamental origins of geometrically controlled mechanomutability are not material specific and the concepts presented here are applicable to the general class of materials with inherent stimulus-responsiveness. Hence, this work can serve as the basis for future studies investigating the role of different and more complex geometries (e.g., kinked, helical, graded, etc.) (Figure 4). The current work holds great potential for tuning stiffness, energy dissipation, load-bearing capability, and penetration resistance and for use in applications sensitive

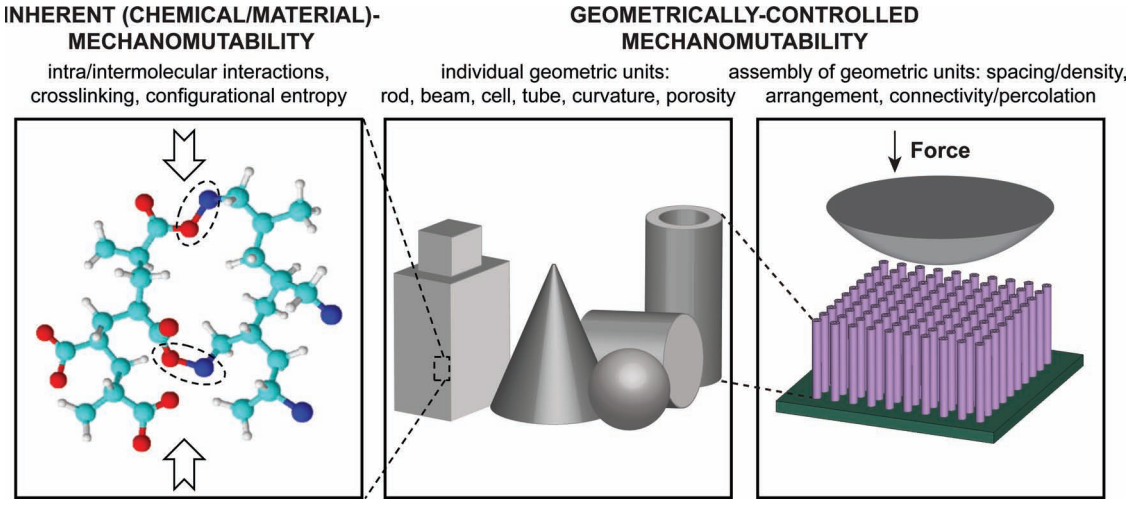

Figure 4. Schematic illustration of the concept of geometrically controlled mechanical responsiveness (mechanomutability).

to mechanical properties, e.g., biosensors, cell adhesion, tissue engineering, and molecular pumps.

Experimental Section

Fabrication and Nanomechanics Experiments: PAH (weight average molecular weight, M_w = 70 000) (Sigma-Aldrich) and PAA (M_w = 90 000, 25% aqueous solution) (Polysciences) tube forests $(PAH7.5/PAA3.5)_X$ (number of bilayers X = 10, 15, and 20) and multilayered film $(PAH7.5/PAA3.5)_{70}$ were assembled at pH 7.5 and 3.5 polyelectrolyte solutions, as described previously.[15,18] The heights and diameters of the tube arrays were measured via fluorescence microscopy.[15] The thickness of the planar film was measured via selective film removal and contact mode atomic force microscopy[25] (Table 1).

Displacement-controlled nanoindentation and force relaxation experiments were conducted via the indenter mode of the 3D Molecular Force Probe (MFP-3D, Asylum Research). Indentation was conducted at constant loading and unloading rates (0.1–10 μm s^{-1}) by adjusting the *z*-piezo displacement rate to compensate for the cantilever bending. For the force relaxation, constant indentation depth was maintained during the 1-min holding period in a similar manner. All of the experiments were performed in pH 2.0 (0.01 M HCl) and 5.5 (0.01 M NaCl) aqueous solutions via gold-coated polystyrene colloidal probe tips (end radius R = 22.5 μm, nominal spring constant $k \approx 14$ N m^{-1}, Novascan), functionalized with neutral, hydrophilic, hydroxyl-terminated self-assembled monolayer by 24 h immersion in 3 mM 11-mercaptoundecanol ($HS(CH_2)_{11}OH$, Sigma-Aldrich) ethanol solution, which was assumed infinite modulus (≈4 GPa)[26] compared to the tested material. Indentation force curves were analyzed using MATLAB R2009a (MathWorks). For each indentation curve, the initial contact point between the probe tip and the PEM was determined via an algorithm reported previously for soft materials in the absence of attractive interactions.[27,28] The effective indentation moduli, E_{ind}, were calculated via the finite thickness substrate-corrected Hertz model,[19] assuming indentation on a homogeneous layer. As E_{ind} varied by several orders of magnitude at different pH values, the average indentation depths during force relaxation at similar maximum force (≈1.2 μN at 1 μm s^{-1} indentation depth rate) were 14 nm for the film at pH 5.5, 181 nm for the tube forest (20 BL) at pH 5.5, 796 nm for the film at pH 2.0, and 884 nm for the tube forest (20 BL) at pH 2.0. One-way repeated measure analysis of variance was applied to study the effect of indentation rate, where significant rate dependence of E_{ind} was found for all the systems ($p < 0.001$). The unpaired student's *t*-test was applied to study the effect of geometry and pH, both of which were found to significantly affect E_{ind} at all the tested rates ($p < 0.01$), except for E_{ind} between the 20-bilayer tube forest and the film at pH 2.0.

Finite Element Analysis: For the planar film, the stress distribution upon indentation was simulated via an axisymmetric FEA nanoindentation model using a rigid spherical indenter with the same radius as the experiment (R = 22.5 μm). At each indentation rate, the indented samples were modelled as isotropic elastic materials using four-node axisymmetric elements in ABAQUS. Large-deformation theory and frictionless contact between the indenter and material were assumed, given the absence of tip–sample adhesion and low friction coefficient measured via lateral force microscopy experiment (data not shown). For the tube forests, a nonlinear FEA was used to analyze the mechanics of deformation by the same indenter, considering rough friction between neighboring tubes upon contact. At each indentation rate, the tubes were modelled with the same inherent material properties as the film at the same strain rate. The mechanical behavior of the individual hollow ("empty") tubes were indeed captured by an "effective model" of a solid ("full") cylinder whereby the geometrical parameters and mechanical properties together provided the equivalent mechanical behavior and deformation mechanisms (i.e., compression, bending, and buckling) of the hollow tubes. The validity of this assumption was discussed previously (Equations (4), (13), and (18) of ref. [13]). The dominant parameter controlling the mechanical behavior of the individual hollow tubes was the cross-sectional area, which was measured experimentally (Table 1) and utilized directly in the effective solid cylinder model. It is noted that the 20 BL system was closest to a solid cylinder with the cross-sectional area ≈92% and the moment of inertia ≈99% of a full rod with the same outer diameter at both pH values tested. The force-indentation depth behavior of the tube forests was simulated separately at pH 5.5 and 2.0 with the experimentally measured tube forest geometrical parameters. The force-depth behavior of indentation into tube forests was a depth-dependent behavior governed by compression, bending, and buckling of the tubes. The simulated force-indentation depth curves were then subjected to substrate-corrected Hertz model[19] to calculate the effective indentation modulus and mechanomutability (Figure 1e). In addition, parametric studies on mechanomutability were conducted using the same protocol with varying tube forest geometrical parameter and the same inherent material properties at 1 μm s^{-1} indentation depth rate (Figure 2b).

Acknowledgements

The authors gratefully acknowledge support of the National Science Foundation MIT Center for Materials Science and Engineering

(DMR-0819762), the MIT Institute for Soldier Nanotechnologies (Army Research Office: Contract W911NF-07-D-0004), the National Security Science and Engineering Faculty Fellowship (N00244–09–1–0064), and the MIT Nanomechanical Technology Laboratory (Dr. A. F. Schwartzman) for technical assistance. They also thank Dr. K. J. Van Vliet and Z. I. Kalcioglu (MIT) for carrying out preliminary experiments and data and Prof. A. J. Grodzinsky (MIT) for helpful discussions.

Received: July 29, 2011
Published online: September 15, 2011

[1] T. P. Russell, *Science* **2002**, *297*, 964.
[2] M. A. Cohen Stuart, W. T. S. Huck, J. Genzer, M. Müller, C. Ober, M. Stamm, G. B. Sukhorukov, I. Szleifer, V. V. Tsukruk, M. Urban, F. Winnik, S. Zauscher, I. Luzinov, S. Minko, *Nat. Mater.* **2010**, *9*, 101.
[3] A. Sidorenko, T. Krupenkin, A. Taylor, P. Fratzl, J. Aizenberg, *Science* **2007**, *315*, 487.
[4] N. A. Peppas, *MRS Bull.* **2006**, *31*, 888.
[5] D. Mertz, J. Hemmerlé, J. Mutterer, S. Ollivier, J.-C. Voegel, P. Schaaf, P. Lavalle, *Nano Lett.* **2007**, *7*, 657.
[6] D. Mertz, C. Vogt, J. Hemmerlé, J. Mutterer, V. Ball, J.-C. Voegel, P. Schaaf, P. Lavalle, *Nat. Mater.* **2009**, *8*, 731.
[7] B. Ozbas, J. Kretsinger, K. Rajagopal, J. P. Schneider, D. J. Pochan, *Macromolecules* **2004**, *37*, 7331.
[8] G. Y. Zhou, Q. Wang, *Proc. SPIE* **2005**, *5760*, 226.
[9] M. Lemieux, D. Usov, S. Minko, M. Stamm, H. Shulha, V. V. Tsukruk, *Macromolecules* **2003**, *36*, 7244.
[10] T. Hugel, N. B. Holland, A. Cattani, L. Moroder, M. Seitz, H. E. Gaub, *Science* **2002**, *296*, 1103.
[11] D. J. Schmidt, F. Ç. Cebeci, Z. I. Kalcioglu, S. G. Wyman, C. Ortiz, K. J. Van Vliet, P. T. Hammond, *ACS Nano* **2009**, *3*, 2207.
[12] N. Holten-Andersen, M. J. Harrington, H. Birkedal, B. P. Lee, P. B. Messersmith, K. Y. C. Lee, J. H. Waite, *Proc. Natl. Acad. Sci. USA* **2011**, *108*, 2651.
[13] L. Wang, C. Ortiz, M. C. Boyce, *J. Eng. Mater. Technol.* **2011**, *133*, 011014.
[14] J. D. Mendelsohn, C. J. Barrett, V. V. Chan, A. J. Pal, A. M. Mayes, M. F. Rubner, *Langmuir* **2000**, *16*, 5017.
[15] K.-K. Chia, M. F. Rubner, R. E. Cohen, *Langmuir* **2009**, *25*, 14044.
[16] L. Zhai, F. Ç. Cebeci, R. E. Cohen, M. F. Rubner, *Nano Lett.* **2004**, *4*, 1349.
[17] J. Hiller, J. D. Mendelsohn, M. F. Rubner, *Nat. Mater.* **2002**, *1*, 59.
[18] D. Lee, R. E. Cohen, M. F. Rubner, *Langmuir* **2007**, *23*, 123.
[19] E. K. Dimitriadis, F. Horkay, J. Maresca, B. Kachar, R. S. Chadwick, *Biophys. J.* **2002**, *82*, 2798.
[20] M. A. Biot, *J. Acoust. Soc. Am.* **1956**, *28*, 168.
[21] E. Pines, W. Prins, *Macromolecules* **1973**, *6*, 888.
[22] J. Choi, M. F. Rubner, *Macromolecules* **2005**, *38*, 116.
[23] H. J. Qi, K. B. K. Teo, K. K. S. Lau, M. C. Boyce, W. I. Milne, J. Robertson, K. K. Gleason, *J. Mech. Phys. Solids* **2003**, *51*, 2213.
[24] S. Pathak, Z. G. Cambaz, S. R. Kalidindi, J. G. Swadener, Y. Gogotsi, *Carbon* **2009**, *47*, 1969.
[25] S. Yamamoto, M. Ejaz, Y. Tsujii, M. Matsumoto, T. Fukuda, *Macromolecules* **2000**, *33*, 5602.
[26] P. H. Mott, J. R. Dorgan, C. M. Roland, *J. Sound Vibrat.* **2008**, *312*, 572.
[27] D. C. Lin, E. K. Dimitriadis, F. Horkay, *J. Biomech. Eng.* **2007**, *129*, 430.
[28] L. Han, E. H. Frank, J. J. Greene, H.-Y. Lee, H.-H. K. Hung, A. J. Grodzinsky, C. Ortiz, *Biophys. J.* **2011**, *100*, 1846.